

Nanoscale Advances

Accepted Manuscript

This article can be cited before page numbers have been issued, to do this please use: C. Kumar, S. Bhattacharjee and S. Srivastava, *Nanoscale Adv.*, 2024, DOI: 10.1039/D4NA00280F.



This is an Accepted Manuscript, which has been through the Royal Society of Chemistry peer review process and has been accepted for publication.

Accepted Manuscripts are published online shortly after acceptance, before technical editing, formatting and proof reading. Using this free service, authors can make their results available to the community, in citable form, before we publish the edited article. We will replace this Accepted Manuscript with the edited and formatted Advance Article as soon as it is available.

You can find more information about Accepted Manuscripts in the [Information for Authors](#).

Please note that technical editing may introduce minor changes to the text and/or graphics, which may alter content. The journal's standard [Terms & Conditions](#) and the [Ethical guidelines](#) still apply. In no event shall the Royal Society of Chemistry be held responsible for any errors or omissions in this Accepted Manuscript or any consequences arising from the use of any information it contains.

Shape anisotropy induced jamming of nanoparticles at liquid interface: A tensiometric study

Chandan Kumar,^{†,‡} Suman Bhattacharjee,^{¶,‡} and Sunita Srivastava^{*,‡}

[†]*Department of Materials Science and Engineering, Nagoya University, Nagoya, 464-8603, Aichi, Japan*

[‡]*Soft Matter and Nanomaterials Laboratory, Department of Physics, Indian Institute of Technology Bombay, Mumbai-400 076, India*

[¶]*Centre for Research in Nanotechnology & Science (CRNTS), Indian Institute of Technology Bombay, Mumbai-400 076, India*

E-mail: sunita.srivastava@phy.iitb.ac.in

Phone: +91-22-2576-7572



Abstract

The intersection of nanotechnology and interfacial science has opened up new avenues for understanding complex phenomena occurring at liquid interfaces. The assembly of nanoparticles at liquid/liquid interfaces provides valuable insights into their interactions with fluid interfaces, essential for various applications, including drug delivery. In this study, we focus on the shape and concentration effect of nanoscale particles towards interfacial affinity. Using pendant drop tensiometry, we monitor the real-time interfacial tension between an oil droplet and an aqueous solution containing nanoparticles. We measure two different types of nanoparticles: spherical gold nanoparticles (AuNPs) and anisotropic gold nanorods (AuNRs), each functionalized with surfactants to facilitate interaction at the interface. We observe that the interface equilibrium behaviour is mediated by kinetic processes, namely, diffusion, adsorption and rearrangement of particles. For anisotropic AuNRs, we observe shape-induced jamming of particles at the interface, evidenced by their slower diffusivity and invariant rearrangement rate. In contrast, the adsorption of spherical AuNPs is dynamic and requires more time to reach equilibrium, indicating weaker interface affinity. By detailed analysis of the interfacial tension data and interaction energy calculations, we show that anisotropic particle shape acquires stable equilibrium inter-particle separation as compared to the isotropic particles. Our findings demonstrate that anisotropic particles are a better design choice for drug delivery applications as it provides better affinity for fluid interface attachment, a crucial requirement for efficient drug transport across cell membranes. Additionally, anisotropic shapes can stabilize interfaces at low particle concentrations as compared to isotropic particles, thus minimizing side effects associated with biocompatibility and toxicity.



1 Introduction

2 The self-assembly of molecules at liquid interfaces drives an interesting range of phenomena
3 observed in complex fluid systems. The properties of liquid interfaces, particularly their
4 tunable surface tension, self-assembly capabilities, and controlled confinement have enabled
5 surface engineering for optimal interfacial behavior. These advantageous features enable the
6 formation of precisely shaped microfluidic droplets, tailored for delicate fluid manipulation
7 within microfluidic devices and lab-on-a-chip technologies,¹ plasmonic nanocrystalline films
8 with enhanced light-matter interactions for improved sensing and optoelectronic applica-
9 tions.^{2,3} Understanding the mechanisms behind interfacial processes drives both fundamen-
10 tal and applied research on the assembly of solids at liquid interfaces. The success of many
11 scientific and technological applications, such as water filtration, biomolecular separation,^{4,5}
12 revolve around the phenomena occurring at the interface between two immiscible liquids,
13 such as oil and water.⁶ Further, fluid interfaces through the mixing of two immiscible liquids
14 are of great interest because of its resemblance to living cell membranes and providing model
15 systems for the study of protein-biomolecule adsorption to such interfaces.⁷ In biomedical ap-
16 plications, many natural delivery systems, such as viruses and blood cells possess anisotropic
17 shapes, thus understanding the nanoscale interaction mechanisms of anisotropic structures
18 with model biological fluid interfaces is crucial. Studies reveal that anisotropic particles are
19 more effective than spherical nanocarriers in terms of membrane binding and drug efficacy,
20 although the nanoscale interaction mechanisms require further investigation,^{8,9} which is the
21 focus of this work.

22 The adsorption of nanostructure at the interface advances through several stages, includ-
23 ing diffusion-limited adsorption, cooperative displacement of particles, and rearrangement
24 to attain an equilibrium position and optimal density.^{1,10,11} These interfacial processes can
25 induce structural changes at the interface, impacting particle adsorption and liquid/liquid
26 interactions, which emanate from a diverse array of self-assembled microstructures.¹²⁻¹⁴ The
27 dynamics of this process are significantly influenced by the particle shape and size,¹⁵ mass



1 loading,¹⁶ and surfactant concentration at the interface.¹⁷ In the nano-regime, the interface
2 binding energy is comparable to thermal energy, resulting in a dynamic adsorption and des-
3 orption process occurring at the same time. This creates instability at the interface, leading
4 to non-equilibrium states with different mechanisms for nanoparticle adsorption. However, it
5 is possible to increase particle binding affinity to the interface through design manipulation.
6 The size, shape, and concentration of nanoparticles significantly influence the adsorption
7 mechanism due to their impact on binding energy.¹⁸

8 Upon adsorption, isotropic nanoparticles tend to form uniform, closely packed monolay-
9 ers due to their symmetrical shape. In contrast, anisotropic particles exhibit more complex
10 adsorption behaviors influenced by their shape anisotropy. For instance, rod-shaped parti-
11 cles may align parallel to the interface,¹⁹ while disk-shaped particles may orient themselves
12 to maximize interfacial contact.²⁰ The initial nanoparticle positional configuration at the
13 interfaces significantly impacts subsequent processes such as rearrangement and jamming,
14 which may arise due to restricted degree of freedom in densely packed systems. The jamming
15 threshold and resulting structure are highly reliant on particle shape anisotropy and size.
16 Isotropic particles rearrange in a relatively straightforward manner, whereas anisotropic par-
17 ticles can form more intricate and varied structures due to their directional interactions and
18 orientations.²¹ It is evident that size and shape-dependent adsorption significantly impact the
19 overall thermodynamic, mechanical, and interactive properties of liquid-liquid interfaces.^{22–24}

20 Fluid interface geometry has been crucial in exploring the regime of tunable solidification,
21 attracting interest for elucidating assembly principles in jammed and liquid states.²⁵ The
22 Langmuir-Blodgett (LB) technique allows precise control over surface pressure, enabling the
23 formation of uniform and densely packed monolayers.²⁶ This method, while advantageous
24 at air-water interfaces, has limitations for studies focused on the liquid-liquid interfaces.
25 Fluctuations due to the dynamic nature of both liquids hinder the formation of uniform
26 monolayers. These challenges necessitate alternative methods for manipulating monolayers
27 at the water-oil interface.^{27,28} Several techniques for measuring interfacial tension have been



1 proposed,²⁹ with pendant drop tensiometry emerging as one of the most simple, robust,
2 and versatile methods for unraveling the complex nature of particle-laden liquid-liquid inter-
3 faces.^{27,30–32} This method allows researchers to control the interfacial area and surrounding
4 environment, enabling them to investigate nanostructure adsorption behavior at liquid-liquid
5 interfaces, advancing material design, targeted drug delivery, and microfluidics.

6 We utilize the pendant drop method to investigate how the shape anisotropy of nanoscale
7 particles affects interfacial tension at the oil-water interface. Further, we explore the interplay
8 between nanoparticle morphology and concentration on their interaction mechanisms at the
9 liquid-liquid interface. The analysis reveals a novel kinetic effect induced by the jamming of
10 anisotropic nanoparticles. Compared to anisotropic particles, isotropic nanoparticles exhibit
11 weaker interfacial affinity, requiring longer adsorption times and higher concentrations for
12 effective binding at the interface. Detailed analysis of interfacial tension data and interaction
13 energy calculations demonstrate that anisotropic particle shape provides a superior driving
14 force for interfacial attachment compared to isotropic particles. Our findings suggest that
15 anisotropic particles are a better design choice for drug delivery applications due to their
16 superior affinity for fluid interface attachment, which is crucial for efficient drug transport
17 across cell membranes.

18 Experimental Section

19 Chemicals

20 Gold (III) chloride trihydrate ($HAuCl_4 \cdot 3H_2O$, $\geq 99.9\%$), Dodecane ($C_{12}H_{26}$, $\geq 99\%$), Trisodium
21 citrate dihydrate ($C_6H_5Na_3O_7 \cdot 2H_2O$, $\geq 99.0\%$), Silver nitrate ($AgNO_3$, $\geq 99.0\%$) are ob-
22 tained from Sigma Aldrich. Hexadecyltrimethylammonium bromide/CTAB ($C_{19}H_{42}BrN$, $>$
23 98%), Sodium borohydride ($NaBH_4$, $> 96\%$) and L-ascorbic acid ($C_6H_8O_6$, $> 99\%$) were
24 purchased from Spectrochem Pvt Ltd (India). 5-Bromosalicylic Acid ($C_7H_5BrO_3$, $> 98.0\%$)
25 was obtained from TCI. Nitric acid (HNO_3) and hydrochloric acid (HCl) of EMAPRTA



1 grade (Merck), were used for the preparation of Aqua Regia. Deionized (DI) water (resistiv-
2 ity $18.2\text{ M}\Omega\text{cm}$) is used for all experiments.

3 Nanoparticle synthesis of different shapes

4 The interfacial studies are performed with particles of two different shapes: isotropic spheri-
5 cal gold nanoparticles (AuNP) and anisotropic gold nanorods (AuNR). The nanoscale parti-
6 cles are synthesized using the improvised protocol developed earlier based on seed-mediated
7 growth process.^{21,33,34}

8 For AuNR, firstly a seed solution of spherical gold nanoparticles were prepared using 5 mL
9 of 0.2 M CTAB solution mixed with HAuCl_4 (0.5 mM, 5 mL). Freshly prepared 600 μL of
10 0.1 M ice cold NaBH_4 is added to the solution under vigorous stirring. For growth solution,
11 45 mL of 0.2 M CTAB and HAuCl_4 (5 mM, 9 mL) is mixed with 112.5 μL of both 0.1 M
12 AgNO_3 and 1.22 M HCl, in that order. Temperature is kept at 30°C for the growth. Freshly
13 made ascorbic acid (10 mM, 5.5 mL) is added to the growth solution under vigorous stirring,
14 followed by 75 μL of seed solution (aged 30 minutes after preparation). The growth solution
15 is incubated overnight at 30°C which leads to the formation of highly monodisperse AuNRs.
16 For AuNPs, citrate capped seeds are prepared first, which in turn produces CTAB capped
17 larger nanoparticles by ligand exchange. First, Freshly prepared 300 μL of ice cold NaBH_4
18 (0.1 M) is added to a 10 mL solution of 0.25 mM HAuCl_4 and sodium citrate. This seed
19 solution is incubated for 2 hours at room temperature. Meanwhile a growth solution con-
20 taining 80 mM CTAB and 0.25 mM gold is prepared. Temperature can be raised upto 50°C
21 to dissolve the CTAB faster but must be cooled down to room temperature before further
22 use. 0.25 mL of 100 mM freshly prepared ascorbic acid is added to 45 mL of growth solution
23 under vigorous stirring, followed by addition of 5 mL of the seed. Stirring is continued for
24 10 minutes till the solution turns dark red. The solution is incubated overnight at room
25 temperature. In both cases, the growth solutions are centrifuged twice at 12000 rpm for 15
26 minutes to remove excess CTAB and other contaminants.



1 All the glassware used for synthesis are washed with Aqua Regia ($HNO_3 : HCl = 1 : 3$)
2 and thoroughly rinsed with DI water and oven-dried. Surfactant, CTAB, is used for surface
3 coating of both the spherical and rod shaped particles for stability of colloidal suspensions,
4 giving them a net positive surface charge. The particle's size and shape characterizations
5 are illustrated in detail in Figure S1 in the *ESI*†.

6 Measurement of interfacial tension

7 A pendant drop at equilibrium is defined by the Young–Laplace equation, establishing a
8 connection between the Laplace pressure across an interface, the curvature of the interface,
9 and the interfacial tension, γ :²⁷

$$\gamma\left(\frac{1}{r_1} + \frac{1}{r_2}\right) = \Delta p. \quad (1)$$

10 Here r_1, r_2 are the principal radii of curvature. The Laplace pressure across the interface is
11 defined as, $\Delta p \equiv \Delta p_0 - \Delta \rho g z$. Δp is the difference in pressure at $z = 0$ and a hydrostatic
12 pressure ($\rho g z$). $\Delta \rho$ represents the density difference between the drop material, (ρ_d), and
13 the bulk phase (ρ_c), and g represents the acceleration due to gravity.

14 The estimate of the surface/interface tension value in an experiment is obtained by a ge-
15 ometrical fit of the drop. While the theoretical formalism for pendant drop is relatively
16 simple, its application to experimental data involves a sophisticated computational workflow
17 to achieve precise alignment between experimental images and the Young-Laplace equation.
18 This workflow comprises two distinct stages: primary image analysis to extract the drop
19 profile, followed by iterative optimization to determine the optimal physical parameters that
20 accurately model the extracted profile. OneAttention (Biolin Scientific) software is utilized
21 for both image processing and numerical optimization to estimate the interface tension pro-
22 file for the pendant drop in our experiments, given in equation 1. One of the most critical
23 steps to obtain an accurate estimate of interface tension is the optimization of the droplet's
24 volume. The ratio between the gravitational force and the surface tension force acting on



1 a drop is given by Bond number, $B = \Delta\rho gL/\gamma$, where $\Delta\rho$ is the density difference for the
2 two fluids, g is the gravitational acceleration, L is a characteristic dimension for the drop
3 and γ is the interfacial tension. For low Bond number systems, this method has well-known
4 limitations. Hence, optimization has been done to adjust the volume of the pendant drop
5 using water such that a stable $\gamma \sim 72 \text{ mN/m}$ is obtained. In a system involving two fluids,
6 the primary criterion is that the fluids are not miscible. It is also beneficial to have a high
7 initial interfacial tension because this generates a large driving force at the interface which
8 promotes the nanoparticle assembly. In pendant drop experiments, a J -shaped needle is used
9 to form a suspended droplet. The density of liquid forming the droplet is lower than the
10 density of the surrounding dispersion liquid, which ensures that a stable suspended droplet
11 is formed at the end of the needle. The interfacial surface tension profile of the suspended
12 drop at the oil-water interface is monitored using Biolin Thetaflex optical tensiometer. In
13 a typical experiment, an inverted drop of dodecane ($15 \pm 1 \mu\text{L}$) is created inside a glass
14 cuvette filled with 6 mL of DI water (subphase). Estimation of the number of nanoparti-
15 cles required to form a complete layer on the droplet's surface (before overcrowding occurs
16 at the oil/water interface) has been done to identify the minimum experimental concentra-
17 tion of the nanoparticles. The subphase phase is exchanged with the desired nanoparticle
18 (AuNR/AuNP) solution for respective experiments.

19 Results and Discussion

20 Size and shape of colloids in suspension

21 The size estimate and shape determination of the freshly synthesized colloidal particles,
22 AuNRs and AuNPs, are obtained from high-resolution TEM images [Figure S1]. Length (L)
23 and diameter (D) of colloidal AuNRs are $\sim 63.5 \pm 4.0 \text{ nm}$ and $\sim 15.4 \pm 1.6 \text{ nm}$, respectively,
24 resulting in anisotropic rod with aspect ratio, (L/D) of ~ 4 . The average size for spherical
25 particles is calculated as $16.1 \pm 1.5 \text{ nm}$, suggesting the formation of highly monodisperse



1 particles.

2 The UV-vis absorption spectroscopy data of anisotropic AuNRs exhibits two distinct plas-

3 mon resonance bands [Figure S2(a)] at 508 nm and 819 nm, corresponding to the surface

4 plasmon oscillations along transverse and longitudinal axes, respectively. As gold nanoparti-

5 cles grow and change their morphology, their surface plasmon absorption peaks also change.

6 The plasmon absorption band for CTAB capped AuNP is 525 nm [Figure S2(b)].

7 Figure S3 and S4 depict the hydrodynamic size distribution and surface potential estimates

8 of the colloids as determined by dynamic light scattering (DLS) and zeta potential measure-

9 ments. The zeta potential estimates for AuNRs and AuNPs were obtained as $\sim +49$ mV

10 and $\sim +38$ mV, respectively. The positively charged surfactant (CTA⁺Br⁻), adsorbs on

11 the colloid's surface providing stability via repulsive forces. In DLS measurements, the hy-

12 drodynamic size is estimated using the Stokes-Einstein equation, which assumes spherical

13 particles. For anisotropic AuNRs two peaks in the DLS data are observed experimentally,

14 due to diffusion corresponding to long and short axis of the rods. For non-spherical particles,

15 DLS can only approximate one dimension (a peak at ~ 61 nm), and the rotational degree of

16 freedom of the particles can lead to unwanted peaks in the DLS data,³⁵ as shown in Figure

17 S3(a). It can be seen in Figure S4, that the hydrodynamic size of CTAB capped AuNP is

18 ~ 31 nm, which is nearly twice the size determined by TEM. This confirms that CTAB

19 ligands are grafted on the surface of the nanoparticle resulting in an effective increase in the

20 size of AuNPs.

21 Nanoparticles at the oil-water interface

22 The pendant drop method is an effective way to measure the tension of colloidal suspensions

23 at the surfaces and interfaces.²⁷ It uses an automated methodology to capture the drop's

24 image, detect edges, perform fit to Young-Laplace equation, and determine the interfacial

25 tension profile as a function of time^{36,37} The interfacial tension profile for systems consisting

26 of colloidal suspension of rods and spherical particles are shown in Figure 1(a,b), respectively.



- 1 The bare dodecane and water interface exhibits interfacial tension, $\gamma_0 \sim 50 \text{ mN/m}$, and is
- 2 stable over time.

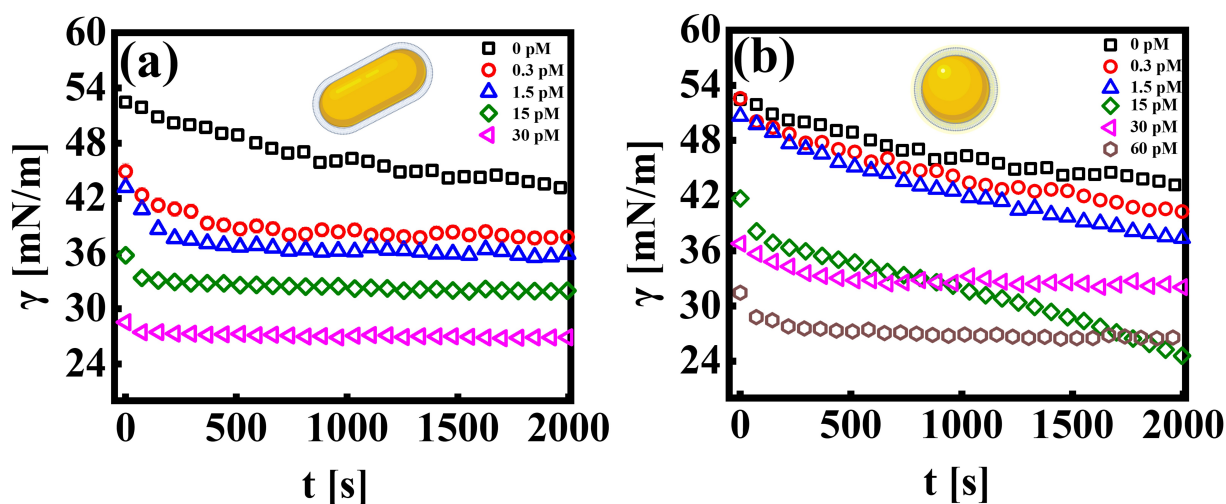


Figure 1: Oil-water interfacial tension profile, $\gamma(t)$ vs t for (a) Nanorods (AuNRs) and (b) Spherical particles (AuNP), dispersed in the water subphase. The $t = 0$, corresponds to the time at which the set volume of oil drop is formed inside the subphase, with the desired particle concentration, as indicated in the legends.

3 Let us first discuss the experimental data from the pendant drop measurements, that
 4 investigate the influence of nanoparticle shape (rod and sphere) on the dynamic interfacial
 5 tension profile as a function of time ($\gamma = \gamma(t)$). The addition of nanoparticles in the sub-
 6 phase results in an exponential decay of the interfacial tension profile at short times, followed
 7 by a quasi-equilibrium state, wherein the interfacial tension value reaches a plateau at large
 8 time. This constant value in the γ vs t profile, signifies that the interface has attained
 9 a maximum nanoparticle coverage at a given concentration. All experiments are recorded
 10 for a measurement time of ~ 2000 seconds. The measurement time was carefully chosen
 11 to avoid error in data due to mechanical stability at longer times. It is observed that the
 12 time taken by the interface to reach an equilibrium value in γ decreases with an increase in
 13 particle concentration. As can be seen in Figure 1(a), at the lowest concentration of AuNR
 14 ($C_R \sim 0.3 \text{ pM}$), γ attends a saturation value after a period of $\sim 300 - 400$ seconds, whereas
 15 at $C_R \sim 30 \text{ pM}$, the γ vs t profile exhibits saturation almost instantaneously.
 16 While both the nanoparticle systems, AuNPs and AuNRs, exhibit qualitatively similar γ vs t



1 profile, they reach a plateau in γ (indicating a saturated interface), at different concentra-
2 tions, as shown in Figure 1(b). For AuNP system at all concentration, $C_S < 30 \text{ pM}$, the
3 interface tension continuously decreases, suggesting that the nanoparticles haven't fully cov-
4 ered the interface, within the measured time frame. For $C_S \geq 30 \text{ pM}$, we measure, $\gamma \text{ vs } t$
5 profile where the interfacial tension reaches a plateau similar to that of AuNR system ob-
6 served at lower concentration $C_R \simeq 15 \text{ nM}$. We further performed the measurement at
7 even higher concentration ($C_S \simeq 60 \text{ pM}$) and found that the saturation observations are
8 consistent by measuring the $\gamma \text{ vs } t$ profile with a plateau. This reinforces the observation
9 that AuNRs are significantly more efficient at lowering and stabilizing the interfacial tension
10 at comparatively lower concentrations compared to AuNPs. Nanoparticle adsorption at an
11 interface reduces interfacial tension, with the magnitude of this decrease proportional to the
12 extent of nanoparticle coverage.³⁸ To infer the nanoparticle coverage at different nanopar-
13 ticle concentrations, we calculate the change in interfacial tension, $\Delta\gamma_{io} (= \gamma_i - \gamma_0)$, which
14 is the difference between the initial interfacial tension of the dodecane-AuNR/NP system at
15 $t = 0 \text{ s}$ (γ_i) and the bare dodecane-water interface (γ_0) [Figure 2(a)]. For both AuNR and
16 AuNP systems, we measure a negative value of interface tension with respect to the oil-water
17 interface indicating nanoparticle adsorption. Further, the estimate of $|\Delta\gamma_{io}|$ increases with
18 concentration, suggesting that a higher concentration of nanoparticles leads to more particles
19 going to the interface.



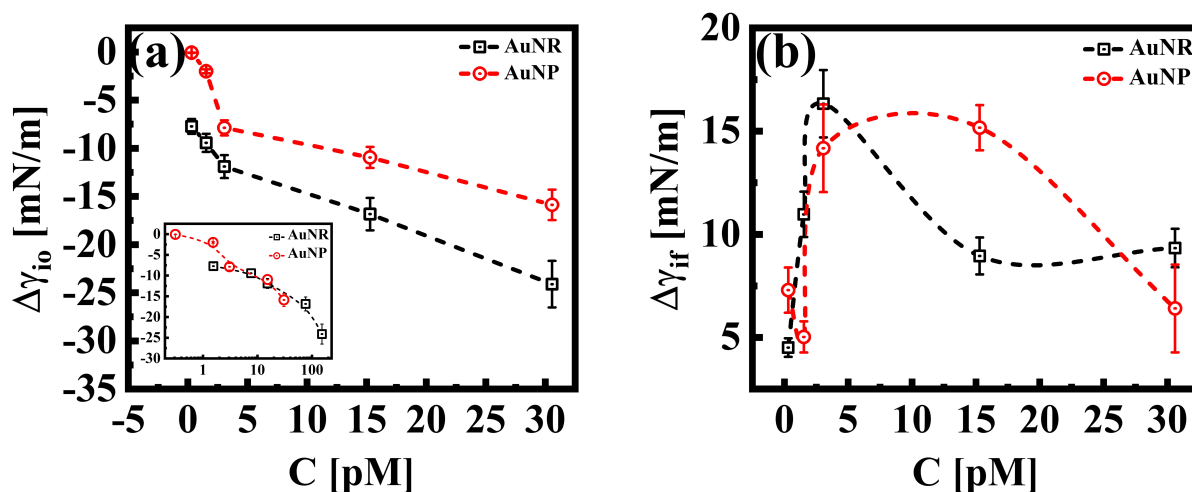


Figure 2: $\Delta\gamma$ vs concentration for AuNP & AuNR at dodecane interface

1 Our results reveal insights into the geometric effect of the nanoparticle shape, with rods
 2 being more effective at lowering the interfacial tension compared to spheres at similar molar
 3 concentrations. To explain this, we show in the inset of Figure 2(a), a $\Delta\gamma_{io}$ vs C plot,
 4 where the concentrations for AuNRs were adjusted to account for their larger surface area
 5 compared to AuNPs (approximately five times larger; $AuNR/AuNP \sim 5$). Interestingly,
 6 the $\Delta\gamma_{io}$ values for both AuNRs and AuNPs (adjusted for surface area) almost perfectly
 7 overlap. This suggests that, since the AuNRs occupy a larger area at the interface compared
 8 to AuNPs, an equivalent number of AuNPs will result in a similar adsorption trend as that
 9 of the AuNRs.

10 In Figure 2(b), we show $\Delta\gamma_{if}$, the difference in the initial interface tension, γ_i , ($t = 0$ s)
 11 and final/equilibrium value, γ_f , (at $t = 2000$ s), obtained from the interfacial tension profiles
 12 in Figure 1. The estimates of $\Delta\gamma_{if}$, reflects the interface saturation and its equilibrium
 13 behavior at varying nanoparticle concentration in the continuous medium. We find that with
 14 increase in concentration, the estimate of $\Delta\gamma_{if}$ increases for both the particle system, followed
 15 by a cross-over behavior where $\Delta\gamma_{if}$ decreases and exhibits constancy, with further increase in
 16 concentration. The saturated interface with maximum coverage, would correspond to smaller
 17 estimates of $\Delta\gamma_{if}$, as such an interface is expected to reach an equilibrium value faster than



1 an unsaturated interface. Thus we can identify the cross over concentration in Figure 2(b),
 2 as the concentration at which the interface approaches maximum coverage. Interestingly
 3 this cross over for AuNR system, occurs at $C_R \approx 3 \text{ pM}$, whereas the same is observed
 4 for AuNP at $C_S > 15 \text{ pM}$. We conclude that in case of AuNR, the maximum coverage
 5 is approached at 5 *fold* smaller concentration as compared to AuNPs. At concentrations
 6 below the cross over concentration, when the interface is not fully saturated, the estimates
 7 of $\Delta\gamma_{if}$ increase with concentration and saturates at an estimate of $\approx 15 \text{ mN/m}$ for both
 8 the systems. At a concentration $\sim 30 \text{ pM}$, we measure similar value of $\Delta\gamma_{if}$ for both shapes
 9 of particles. This suggests that both systems have reached an maximum particle coverage,
 10 where no more particles can bind at the interface.

11 Adsorption kinetics of AuNR and AuNP

12 Nanoparticles adsorb at the liquid/liquid interfaces when they are introduced into a system
 13 containing two different liquids. The differences in interfacial energy between the nanoparti-
 14 cles and the liquids cause the nanoparticles to attach to the interface. The energy associated
 15 with a particle getting trapped in an interface is dependent on the size of the particle, the
 16 orientation of the attachment, and the interfacial tension between the two media. This en-
 17 ergy is termed as the detachment energy, ΔE , of the particle-interface system and is given
 18 by:

$$\Delta E = \pi r^2 \gamma_0 (1 - \cos\theta)^2 \quad (2)$$

19 where r is radius of nanoparticle and θ is the contact angle. The value of $\theta = 90^\circ$ is
 20 taken from literature considering nanoparticle's favorable attachment affinity towards the
 21 oil-water interface.^{39,40} For the anisotropic particle, the radius, r , is approximated to $r_{eff} =$
 22 $r \times \text{shape factor}$. The shape factor for the nanorods is calculated using the area fraction
 23 covered by a spherical particle of the same volume.⁴¹ Higher the value of ΔE , the more
 24 difficult it is to detach the particle from the interface. This is evident from the calculated



1 values as shown in Table 1, where AuNRs possess 8 times higher ΔE compared to AuNPs.
2 The interplay between interfacial tension and pendant drop shape governs both the adsorp-
3 tion kinetics of particles at the interface and the dynamic surface tension. Dynamic interfacial
4 tension, calculated using the Ward-Tordai theory,⁴² is the surface tension that changes over
5 time due to the adsorption or desorption of surface-active agents or other species at the
6 interface. This theory is based on the assumption that the surface-active agent adsorbs at
7 the interface in a monolayer, and the surface tension reduction is proportional to the agent's
8 surface concentration. The initial interfacial tension decay with time due to nanoparticle's
9 diffusion at the interface, can be correlated using a modified Ward and Tordai equation⁴³
10 given by:

$$\gamma(t) = \gamma_i - 2N_A C_0 \Delta E \sqrt{\frac{D_{eff} t}{\pi}}. \quad (3)$$

11 Here, $\gamma(t)$, is the interface tension at time t , γ_i is the initial value of interface tension, N_A is
12 the Avogadro number, C_0 is the concentration of nanoparticles in subphase and D_{eff} is the
13 effective diffusion coefficient. D_{eff} gives a measure of the nanoparticle's diffusion rates from
14 bulk to the interface.

15 The study of diffusion coefficient is important for understanding the transport of molecules
16 or particles across the interface. It has been demonstrated that the adsorption of particles
17 consists of three main kinetic processes: (i) diffusion from the bulk onto the interface, (ii)
18 adsorption (penetration) and interfacial unfolding, and (iii) aggregation within the interfacial
19 layer, as well as the formation of multilayers.⁴⁴ In a specific diffusion process occurring at
20 short time scales (Fickian diffusion), the change in interfacial tension over time follows a
21 square root relationship, $\gamma \sim \sqrt{t}$. In the subphase, the nanoparticles are under constant
22 Brownian motion where the movement of the particles is stochastic. The presence of the
23 interface creates a flux as the particle assumes it like a sink and tends to diffuse towards it.
24 At $t \rightarrow 0$, the nanoparticles moving towards the interface experience only a bare interface.
25 Once, the interface gets crowded with particles, the diffusive nature also changes.⁴⁵ A typical
26 interfacial tension profile for the AuNR system at 0.3 pM , revealing Fickian diffusion is



1 shown in Figure 3(a). The linear portion of the data, extending up to the first change in
 2 slope (indicated by the blue dotted line), is used to estimate the effective diffusion coefficient
 3 (D_{eff}) using equation 3. This confirms that at short time, the nanoparticle's diffusion
 4 process is the dominant factor controlling their adsorption at the interface, as also observed
 5 in previous research.^{43,46,47} Similar behavior was observed in γ vs \sqrt{t} profile for both the
 6 AuNP and AuNR particles at all the different concentrations.

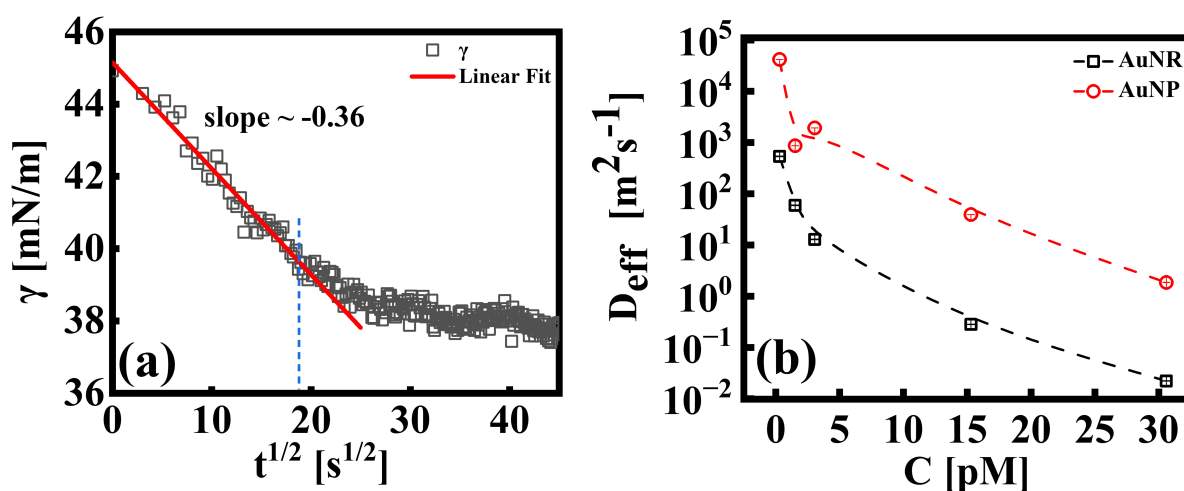


Figure 3: (a) A typical representative plot for γ vs $t^{1/2}$, for a AuNR suspension at 0.3 pM. A linear fit to the data using equation 3 is shown by the extrapolated solid line (up to $t \sim 400s$). The extent of the fitting range is shown via the blue dotted line. (b) Effective diffusion coefficients (D_{eff}), for AuNP and AuNR systems as indicated in the respective legends.

7 In Figure 3(b), we compare the estimates of D_{eff} , that is the diffusion behavior of AuNR
 8 and AuNP particles towards the interface, calculated by fitting equation 3, to the measured
 9 interfacial tension profiles as explained above. At any given concentration, it has been found
 10 that the D_{eff} of AuNP is at least two orders of magnitude higher than that of AuNR. This
 11 difference can be explained by the size and shape of the particles, which play a crucial role in
 12 how easily they move through the liquid. Even though the diameter of the rods are similar
 13 to the diameter of the nanoparticles, the rods are about four times longer. This larger size
 14 and elongated shape make AuNRs experience more drag from the surrounding liquid as they
 15 move, obstructing their diffusion compared to the smaller, spherical AuNPs. Additionally,



1 the larger surface area of AuNRs (around five times that of AuNPs) means that they collide
2 with each other more frequently, further slowing them down. Additionally, it's worth noting
3 that factors such as the shape of the nanoparticles can also influence the effective diffusion
4 coefficient. The AuNRs, owing to their longer axis ($4\times$ longer compared to AuNP size),
5 adsorb to the interface occupying a larger area even for equal particle concentrations. This
6 faster coverage of the interface by AuNRs also hinders their diffusion towards the interface.

7
8 Using the Stoke-Einstein relation ($D_0 = \frac{K_B T}{6\pi\eta r}$) in solution, we have calculated the free
9 diffusion coefficient, (D_0), to obtain an approximate estimate of nanoparticle diffusivity in the
10 dodecane/water interface. Here K_B , T and η represent the Boltzmann constant, temperature
11 of aqueous suspension, and solvent viscosity ($\eta = 0.83$ cP for water), respectively. We
12 estimate D_0 values $\approx 3.53 \times 10^{-11} m^2 s^{-1}$ and $1.35 \times 10^{-11} m^2 s^{-1}$, respectively for AuNP
13 and AuNR. For AuNR, the effective radius, r_{eff} , is used for the calculation of D_0 . It is worth
14 noting that the free diffusivity of AuNP is about $2.7\times$ higher than AuNR.

15 The nanoparticle adsorptions at the interface rapidly form an energy barrier due to collisions
16 between particles that have detached from the interface and those approaching from the bulk.
17 Particles adsorbing at the interface face an energy barrier, U , that determines the effective
18 diffusivity (D_{eff}). Under the influence of U , D_{eff} can be related to D_0 as follows;

$$D_{eff} = D_0 \exp\left(\frac{-U}{K_B T}\right) \quad (4)$$

19 By using equation 4, U was calculated from the D_{eff} values and is presented in Table 1.
20 $D_{eff} \gg D_0$, typically suggests that the nanoparticle is experiencing less hindrance or re-
21 sistance while moving through the medium than predicted by the Stokes-Einstein equation.
22 This can occur due to various factors, such as particle-particle interactions, non-uniform flow
23 fields, and anomalous diffusion behavior.

24



Table 1: Calculated parameters from equations 2,3 and 4

Particle	$C(pM)$	$\Delta E/K_B T$	$U/K_B T$	$D_0(m^2/s^{-1})$	$D_{eff}(m^2/s^{-1})$
AuNP	0.3	2211.07	-34.11	3.53×10^{-11}	2.29×10^4
AuNR	0.3	17688.53	-30.95	1.35×10^{-11}	3.72×10^2
AuNP	30	2211.07	-24.09	3.53×10^{-11}	1.02
AuNR	30	17688.53	-20.86	1.35×10^{-11}	0.02

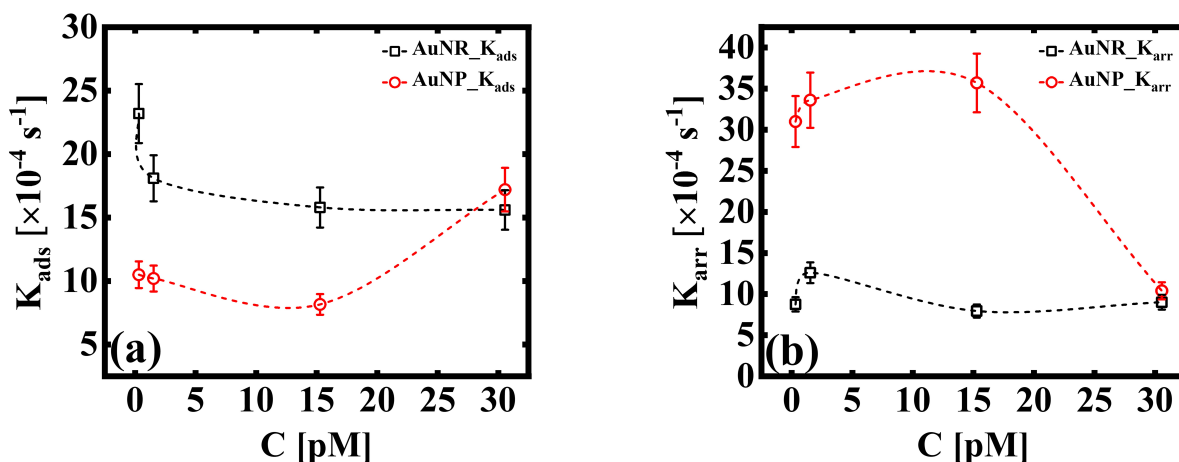


Figure 4: (a) First order adsorption rate, K_{ads} and (b) Molecular rearrangement rate, K_{arr} , of adsorbed particles at the liquid/liquid interface (dashed lines as a guide to the eye). The estimates in (a,b) are obtained using the linear regression model given by eqn 5.

1 To gain deeper insights into these interfacial dynamics that are crucial for understanding
 2 the interaction of nanoparticles with the interface, we utilized the established mathematical
 3 framework proposed by Graham and Phillips. The temporal evolution of this complex be-
 4 havior can be captured by a first-order equation, allowing for quantitative analysis of their
 5 rates,⁴⁸ given by:

$$\ln\left(\frac{\gamma_f - \gamma_t}{\gamma_f - \gamma_i}\right) = -K_i t \quad (5)$$

6 The dynamic surface tension, γ_t , at time, $t = 0$ and $t = 2000$ are denoted by γ_i , and γ_f ,
 7 respectively. K_i is the first order rate constant and calculated by fitting the interfacial tension
 8 data to equation 5. Typically there are two different slopes (Figure S5); the initial slope



1 ($K_i \equiv K_{ads}$), represents the rate at which molecules adsorb to the liquid/liquid interface,
2 while the second slope ($K_i \equiv K_{arr}$) corresponds to the rate constant for rearrangement at
3 the interface. In Figure 4, we show the estimates of K_{ads} and K_{arr} , for both the AuNP and
4 AuNR systems, the inverse of which is proportional to time for nanoparticle adsorption and
5 rearrangement at the interface, respectively. Interestingly, the data unravels a fascinating
6 difference in the adsorption and rearrangement time scales of AuNPs and AuNRs, at the
7 interface.

8 For AuNP system at particle concentration $\leq 15 \text{ pM}$, the estimates of K_{ads} , which quan-
9 tifies the tendency of the nanoparticles to bind to the interface, does not change much [Figure
10 4(a)] and stays fairly steady. This suggests that in this concentration regime, particles con-
11 stantly bind and detach from the interface. This continuous exchange keeps the K_{ads} value
12 relatively constant because the rate of attachment is balanced by the rate of detachment.
13 When the concentration of the solution, $C_S \geq 30 \text{ pM}$, we measure an increase in the value
14 of K_{ads} . This suggests that AuNPs are attaching to the interface in a stable way at high
15 concentrations. Conversely, the AuNR system shows a slight decrease in K_{ads} initially (upto
16 $\sim 3 \text{ pM}$), suggesting slow adsorption. As the anisotropic particles adsorb at the interface,
17 the local particle density increases, thus creating a barrier for the incoming particles, with
18 increasing concentration. This can be attribute to shape induced jamming at the interface,
19 prohibiting particle exchange with the medium, an phenomena observed in case of isotropic
20 particles. As the AuNRs occupy approximately five times larger area at the interface com-
21 pared to a spherical AuNP, it is intuitive to assume that the interface becomes saturated
22 with AuNR, even at the lowest concentration. This reduces the effective concentration of
23 the incoming particles at the interface, leading to a decrease in the adsorption coefficient. A
24 constant estimate of K_{ads} with further increase in particle concentration ($C_R \geq 3 \text{ pM}$), indi-
25 cates that their interface binding rate remains relatively unchanged regardless of the particle
26 concentration in the subphase. This invariant K_{ads} with increasing AuNR concentration,
27 can be attributed to the jamming effect. Jamming occurs when adsorbed particles surround



1 and cage the incoming particles, preventing them from accessing the adsorption sites at the
2 interface.

3 These observations suggest that spherical shape of AuNP system results in a more dynamic
4 exchange of particles with the medium, until at very high concentration where interface
5 saturation and equilibrium is achieved. The rate constant corresponding to nanoparticle's
6 rearrangement at the interface is shown in Figure 4(b). We found that K_{arr} for AuNR re-
7 mains invariant for all experimental conditions, which corroborates with the idea of jammed
8 interface due to shape anisotropy, even at small nanoparticle concentrations, where we mea-
9 sure no scope for any dynamic behaviour. In the case of AuNPs, K_{arr} initially shows a
10 high value owing to the dynamic nature of the nanoparticle layer at the interface. K_{arr} falls
11 sharply at $C_S \geq 30 \text{ pM}$, when the interface finally reaches the quasi-equilibrium state.

12 **Calculation of total interactions between AuNPs/AuNRs near the** 13 **interface**

14 Beyond the diffusion-limited regime, the adsorption or rearrangement of the nanoparticles
15 at the interface involves interactions at the nanoscale. The nanoparticles have a positively
16 charged surfactant coating around them and the dodecane interface is negatively charged as
17 reported in literature.⁴⁹ To understand the interaction between the particle and the interface,
18 it is helpful to conceptualize it as an inter-particle interaction occurring in the presence
19 of an interface. These interactions involve the inter-particle van der Waals forces at the
20 interface, as well as the electric double-layer interaction originating from the surface charge
21 of the particles in the vicinity of an oppositely charged interface. Following the DLVO
22 (Derjaguin, Landau, Verwey, and Overbeek) theory of colloidal stability,³⁸ we examined
23 the interaction between two identical spherical particles carrying a fixed surface potential.
24 The total interaction energy, $U_T(h)$, between two spherical particles of radius, r , separated
25 by a distance, h , from each other at the interface, is the sum of the repulsive electrostatic
26 interaction energy, U_{el} , and the attractive van der Waals interaction energy, U_{vdW} . Thus, we



1 have $U_T = U_{el} + U_{vdW}$. The van der Waals interaction between two spherical particles with
2 a flat plate can be written as:

$$U_{vdW} = -\frac{A_H}{6} \left[\left(\frac{2r^2}{h(4r+h)} \right) + \left(\frac{2r^2}{(2r+h)^2} \right) + \ln \left(\frac{h(4r+h)}{(2r+h)^2} \right) \right]. \quad (6)$$

3 Here, A_H is the effective Hamaker constant determined using the mixing rule and depends
4 on the Hamaker constants for the oil, water, and particle. Assuming that the spherical
5 gold particles interact with a dodecane oil slab, the effective Hamaker constant is written
6 as $A_H \approx \sqrt{(A_{oil} - A_{water})} \sqrt{(A_{particle} - A_{water})}$. Here, A_{oil} is the Hamaker constant for
7 dodecane (5×10^{-20} J), A_{water} is the Hamaker constant for water (3.7×10^{-20} J), and
8 $A_{particle}$ is the Hamaker constant for gold (47×10^{-20} J).³⁸ Using this equation, we calculate
9 the effective Hamaker constant to be $A_H = 7.5 \times 10^{-20}$ J, which enables us to determine the
10 van der Waals interaction between the particles at the interface based on the particle radius
11 (r) and the surface-to-surface distance (h). We have considered h values from 0.025 – 15 nm.
12 The electrostatic interaction energy between nanoparticles at the interface is estimated using
13 the formulation given by:

$$U_{el} = 32\pi\epsilon_r\epsilon_0r\left(\frac{k_B T}{e}\right)^2 \tanh^2\left(\frac{e\psi}{4k_B T}\right) e^{-2\kappa h}. \quad (7)$$

14 Here ϵ_r, ϵ_0 are the relative permittivity of the medium and vacuum respectively, k_B is the
15 Boltzmann constant, T is the temperature, κ is the Debye length and ψ is the surface poten-
16 tial of the particles which is approximated to their measured zeta potentials [Figure S3(b),
17 S4(b)]. The total interaction energies, U_T , along with its attractive and repulsive compo-
18 nents, calculated with specific parameters for AuNR and AuNP system are shown in Figure
19 5. The calculations reveal, though both the systems are stabilized at the interface by a
20 repulsive energy barrier, there is a subtle difference in the dependence of U_T . For AuNRs,
21 we measure a minimum in the total energy at an inter-particle separation of $\sim 7 - 8$ nm
22 [Figure 5(a)], indicating an attractive force that contributes to their stability at the inter-



1 face. On the other hand, AuNPs do not experience any inter-particle attractive interaction.
 2 Weak inter-particle repulsion hinders the formation of any kind of stable arrangement. This
 3 indicates that the interaction between the interface and AuNPs are weaker and less specific
 4 in comparison to the interface and AuNRs, potentially leading to a less stable and more
 5 dynamic arrangement for the spherical particles. The stable configuration of AuNRs also
 6 supports the idea that large elongated particles facilitates the formation of jammed structure
 7 at the interface, regardless of the specific concentration used in the experiment.

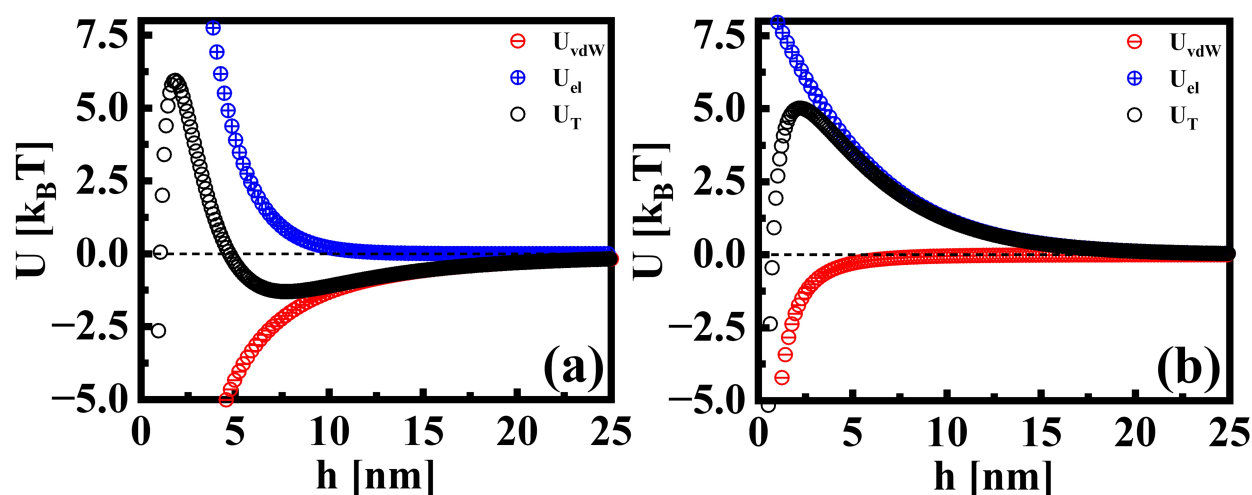


Figure 5: The interaction potentials between particles in presence of a flat interface. The attractive, repulsive, and total interaction energies are shown for (a) AuNR and (b) AuNP.

8 Conclusion

9 In this study, we investigate the shape and concentration effects on the self-assembly mech-
 10 anism of surfactant coated nanoparticles at the liquid/liquid interface. Using pendant
 11 drop tensiometry, we monitor the dynamic interfacial tension, as the spherical AuNPs and
 12 anisotropic AuNRs diffuse towards the interface of a dodecane micro-droplet. We observed
 13 that AuNRs adsorb and create a stable interface layer at all particle concentrations, whereas,
 14 the adsorption of AuNPs is dynamic, with particle exchange from the continuous phase. The
 15 interface establishes a stable AuNP layer at a concentration approximately 100X higher than



1 that required for the AuNRs. The estimates of adsorption and rearrangement coefficients
2 provide insights into the nanoparticles' adsorption kinetics at the interface. We find that
3 AuNRs possess $\sim 3X$ higher adsorption coefficients than AuNPs, suggesting better affinity
4 of the anisotropic particles towards the interface. Further, the rearrangement coefficient for
5 AuNR does not change with concentration. This difference is attributed to the influence
6 of particle's shape and size on their adsorption behavior. Due to the larger surface area,
7 AuNRs effectively cover the interface with a lesser number of particles compared to the
8 smaller, spherical AuNPs. For anisotropic AuNRs, we measure shape-induced jamming of
9 particles at the interface, evidenced by their slower diffusivity and invariant rearrangement
10 rate. The estimates of the interaction energies between the particles near the interface indi-
11 cate that the anisotropic particle shape acquires stable equilibrium inter-particle separation
12 as compared to isotropic particles.

13 To summarize, the findings from current work highlight the impact of shape and concen-
14 tration on nanoparticle interactions at the liquid/liquid interface, contributing to the ad-
15 vancements in understanding the dynamic behavior of nanoparticles at fluid interfaces. We
16 demonstrate that anisotropic particles exhibit enhanced interfacial binding and stable equi-
17 librium inter-particle separation at the interface. This study holds significant importance
18 for optimizing the design of nanoscale carriers in drug delivery applications. Our results
19 indicate that anisotropic nanocarriers offer advantages in fluid interface attachment, a pivot
20 factor in improving drug transport across cellular membranes. The choice of anisotropic par-
21 ticle design may offer additional advantage of bio-imaging, controlled and targeted delivery.
22 Additionally, their ability to stabilize interfaces at lower particle concentrations compared
23 to isotropic particles, can help minimize concerns regarding biocompatibility and toxicity
24 related side effects.





1 Author contributions

2 CK - Conceptualization, Investigation, Methodology, Data Curation, Writing – Original
3 Draft. SB - Investigation, Methodology, Data Curation, Formal Analysis, Writing – Orig-
4 inal Draft, Review & Editing. SS - Conceptualization, Investigation, Supervision, Funding
5 Acquisition, Resources, Validation, Writing – Review & Editing
6 CK and SB contributed equally to the manuscript. All authors have approved the final
7 version of the manuscript.

8 Conflicts of interest

9 The authors declare no conflict of interest.

10 Acknowledgement

11 The authors thank SAIF IITB [FEG-SEM, FEG-TEM(200kV/300kV)] instrument facilities.
12 CK acknowledges IITB. SB acknowledges the financial support from CRNTS, IIT Bombay.
13 SS acknowledges support from CRS-UGC-DAE, India.

14 Supporting Information Available

15 TEM micrographs (with size estimation) of the synthesized nanoparticles, UV-Vis spectra,
16 DLS and Zeta potential data and a representative fitting plot for K_{ads} , K_{arr} are provided in
17 the *ESI*[†].

18 References

- 19 (1) Cui, M.; Emrick, T.; Russell, T. P. Stabilizing liquid drops in nonequilibrium shapes
20 by the interfacial jamming of nanoparticles. *Science* **2013**, *342*, 460–463.

- 1 (2) Lin, Y.; Skaff, H.; Emrick, T.; Dinsmore, A.; Russell, T. P. Nanoparticle assembly and
2 transport at liquid-liquid interfaces. *Science* **2003**, *299*, 226–229.
- 3 (3) Lin, Y.; Böker, A.; Skaff, H.; Cookson, D.; Dinsmore, A.; Emrick, T.; Russell, T. P.
4 Nanoparticle assembly at fluid interfaces: structure and dynamics. *Langmuir* **2005**, *21*,
5 191–194.
- 6 (4) He, J.; Kanjanaboos, P.; Frazer, N. L.; Weis, A.; Lin, X.-M.; Jaeger, H. M. Fabrication
7 and Mechanical Properties of Large-Scale Freestanding Nanoparticle Membranes. *Small*
8 **2010**, *6*, 1449–1456.
- 9 (5) He, J.; Lin, X.-M.; Chan, H.; Vukovic, L.; Král, P.; Jaeger, H. M. Diffusion and filtration
10 properties of self-assembled gold nanocrystal membranes. *Nano Letters* **2011**, *11*, 2430–
11 2435.
- 12 (6) Hua, X.; Bevan, M. A.; Frechette, J. Competitive adsorption between nanoparticles
13 and surface active ions for the oil–water interface. *Langmuir* **2018**, *34*, 4830–4842.
- 14 (7) Huang, X.; Li, M.; Green, D. C.; Williams, D. S.; Patil, A. J.; Mann, S. Interfacial
15 assembly of protein–polymer nano-conjugates into stimulus-responsive biomimetic pro-
16 tocells. *Nature communications* **2013**, *4*, 2239.
- 17 (8) Chen, J.; Clay, N. E.; Park, N.-h.; Kong, H. Non-spherical particles for targeted drug
18 delivery. *Chemical engineering science* **2015**, *125*, 20–24.
- 19 (9) Uhl, C.; Gao, Y.; Zhou, S.; Liu, Y. The shape effect on polymer nanoparticle transport
20 in a blood vessel. *RSC advances* **2018**, *8*, 8089–8100.
- 21 (10) Hua, X.; Frechette, J.; Bevan, M. A. Nanoparticle adsorption dynamics at fluid inter-
22 faces. *Soft matter* **2018**, *14*, 3818–3828.
- 23 (11) Ji, X.; Wang, X.; Zhang, Y.; Zang, D. Interfacial viscoelasticity and jamming of colloidal



- 1 particles at fluid–fluid interfaces: a review. *Reports on Progress in Physics* **2020**, *83*,
2 126601.
- 3 (12) Mendoza, A. J.; Guzmán, E.; Martínez-Pedrero, F.; Ritacco, H.; Rubio, R. G.; Or-
4 tega, F.; Starov, V. M.; Miller, R. Particle laden fluid interfaces: Dynamics and inter-
5 facial rheology. *Advances in Colloid and Interface Science* **2014**, *206*, 303–319.
- 6 (13) Krägel, J.; Derkatch, S. R. Interfacial shear rheology. *Current Opinion in Colloid &*
7 *Interface Science* **2010**, *15*, 246–255.
- 8 (14) Srivastava, S.; Nykypanchuk, D.; Fukuto, M.; Halverson, J. D.; Tkachenko, A. V.;
9 Yager, K. G.; Gang, O. Two-dimensional DNA-programmable assembly of nanoparticles
10 at liquid interfaces. *Journal of the American Chemical Society* **2014**, *136*, 8323–8332.
- 11 (15) Cheng, H.-L.; Velankar, S. S. Film climbing of particle-laden interfaces. *Colloids and*
12 *Surfaces A: Physicochemical and Engineering Aspects* **2008**, *315*, 275–284.
- 13 (16) Dong, L.; Johnson, D. Surface tension of charge-stabilized colloidal suspensions at the
14 water- air interface. *Langmuir* **2003**, *19*, 10205–10209.
- 15 (17) Hadler, K.; Cilliers, J. The effect of particles on surface tension and flotation froth
16 stability. *Mining, Metallurgy & Exploration* **2019**, *36*, 63–69.
- 17 (18) Chai, Y.; Hasnain, J.; Bahl, K.; Wong, M.; Li, D.; Geissler, P.; Kim, P. Y.; Jiang, Y.;
18 Gu, P.; Li, S., et al. Direct observation of nanoparticle-surfactant assembly and jamming
19 at the water-oil interface. *Science advances* **2020**, *6*, eabb8675.
- 20 (19) Eatson, J. L.; Gordon, J. R.; Cegielski, P.; Giesecke, A. L.; Suckow, S.; Rao, A.; Sil-
21 vestre, O. F.; Liz-Marzán, L. M.; Horozov, T. S.; Buzza, D. M. A. Capillary Assembly of
22 Anisotropic Particles at Cylindrical Fluid–Fluid Interfaces. *Langmuir* **2023**, *39*, 6006–
23 6017.



- 1 (20) Kumar, C.; Srivastava, S. Structural and Dynamical Studies of a Lipid–Nanoclay Com-
2 posite Layer at the Air–Water Interface. *Langmuir* **2022**, *38*, 10400–10411.
- 3 (21) Khawas, S.; Bhattacharjee, S.; Mukherjee, S.; Sain, A.; Srivastava, S. Directing the for-
4 mation of tunable superlattice crystalline phases from anisotropic nanoparticles. *Col-
5 loids and Surfaces A: Physicochemical and Engineering Aspects* **2024**, 133762.
- 6 (22) Li, G.; Zuo, Y. Y. Molecular and colloidal self-assembly at the oil-water interface.
7 *Current Opinion in Colloid & Interface Science* **2022**, 101639.
- 8 (23) Helden, L.; Dietrich, K.; Bechinger, C. Interactions of colloidal particles and droplets
9 with water–oil interfaces measured by total internal reflection microscopy. *Langmuir*
10 **2016**, *32*, 13752–13758.
- 11 (24) Anzivino, C.; Chang, F.; Soligno, G.; Van Roij, R.; Kegel, W. K.; Dijkstra, M. Equilib-
12 rium configurations and capillary interactions of Janus dumbbells and spherocylinders
13 at fluid–fluid interfaces. *Soft Matter* **2019**, *15*, 2638–2647.
- 14 (25) Zhang, Z.; Jiang, Y.; Huang, C.; Chai, Y.; Goldfine, E.; Liu, F.; Feng, W.; Forth, J.;
15 Williams, T. E.; Ashby, P. D., et al. Guiding kinetic trajectories between jammed
16 and unjammed states in 2D colloidal nanocrystal-polymer assemblies with zwitterionic
17 ligands. *Science advances* **2018**, *4*, eaap8045.
- 18 (26) Srivastava, S.; Nykypanchuk, D.; Fukuto, M.; Gang, O. Tunable nanoparticle arrays at
19 charged interfaces. *ACS nano* **2014**, *8*, 9857–9866.
- 20 (27) Berry, J. D.; Neeson, M. J.; Dagastine, R. R.; Chan, D. Y.; Tabor, R. F. Measurement
21 of surface and interfacial tension using pendant drop tensiometry. *Journal of Colloid
22 and Interface Science* **2015**, *454*, 226–237.
- 23 (28) Eggers, J.; Villermaux, E. Physics of liquid jets. *Reports on Progress in Physics* **2008**,
24 *71*, 036601.



- 1 (29) Drelich, J.; Fang, C.; White, C. Measurement of interfacial tension in fluid-fluid systems.
2 *Encyclopedia of Surface and Colloid Science* **2002**, *3*, 3158–3163.
- 3 (30) Worthington, A. M. II. On pendent drops. *Proceedings of the Royal Society of London*
4 **1881**, *32*, 362–377.
- 5 (31) Toor, A.; Forth, J.; Bochner de Araujo, S.; Merola, M. C.; Jiang, Y.; Liu, X.; Chai, Y.;
6 Hou, H.; Ashby, P. D.; Fuller, G. G., et al. Mechanical properties of solidifying as-
7 semblies of nanoparticle surfactants at the oil–water interface. *Langmuir* **2019**, *35*,
8 13340–13350.
- 9 (32) Huerre, A.; Cacho-Nerin, F.; Poulichet, V.; Udoh, C. E.; De Corato, M.; Garbin, V.
10 Dynamic organization of ligand-grafted nanoparticles during adsorption and surface
11 compression at fluid–fluid interfaces. *Langmuir* **2018**, *34*, 1020–1028.
- 12 (33) Tang, S.; Li, Y.; Huang, H.; Li, P.; Guo, Z.; Luo, Q.; Wang, Z.; Chu, P. K.; Li, J.;
13 Yu, X.-F. Efficient enrichment and self-assembly of hybrid nanoparticles into removable
14 and magnetic SERS substrates for sensitive detection of environmental pollutants. *ACS*
15 *Applied Materials & Interfaces* **2017**, *9*, 7472–7480.
- 16 (34) Fenger, R.; Fertitta, E.; Kirmse, H.; Thünemann, A. F.; Rademann, K. Size depen-
17 dent catalysis with CTAB-stabilized gold nanoparticles. *Physical Chemistry Chemical*
18 *Physics* **2012**, *14*, 9343–9349.
- 19 (35) Pecora, R. Dynamic light scattering measurement of nanometer particles in liquids.
20 *Journal of nanoparticle research* **2000**, *2*, 123–131.
- 21 (36) Hansen, F.; Rødsrud, G. Surface tension by pendant drop: I. A fast standard instrument
22 using computer image analysis. *Journal of colloid and interface science* **1991**, *141*, 1–9.
- 23 (37) Stetten, A. Z.; Kratz, F. S.; Schilderink, N.; Ayirala, S.; Duits, M. H.; Kierfeld, J.;



- 1 Mugele, F. Elastometry of Complex Fluid Pendant Capsules. *Langmuir* **2023**, *39*,
2 16303–16314.
- 3 (38) Israelachvili, J. N. *Intermolecular and surface forces*; Academic press, 2011.
- 4 (39) Yang, G.; Hallinan, D. T. Gold nanoparticle monolayers from sequential interfacial
5 ligand exchange and migration in a three-phase system. *Scientific reports* **2016**, *6*,
6 35339.
- 7 (40) Guzmán, E.; Ortega, F.; Rubio, R. G. Forces controlling the assembly of particles at
8 fluid interfaces. *Langmuir* **2022**, *38*, 13313–13321.
- 9 (41) Qi, W. H.; Wang, M. P.; Liu, Q. Shape factor of nonspherical nanoparticles. *Journal of*
10 *materials science* **2005**, *40*, 2737–2739.
- 11 (42) Ward, A.; Tordai, L. Time-dependence of boundary tensions of solutions I. The role of
12 diffusion in time-effects. *The Journal of Chemical Physics* **1946**, *14*, 453–461.
- 13 (43) Bizmark, N.; Ioannidis, M. A.; Henneke, D. E. Irreversible adsorption-driven assem-
14 bly of nanoparticles at fluid interfaces revealed by a dynamic surface tension probe.
15 *Langmuir* **2014**, *30*, 710–717.
- 16 (44) Pérez, O. E.; Sánchez, C. C.; Pilosof, A. M.; Patino, J. M. R. Dynamics of adsorption
17 of hydroxypropyl methylcellulose at the air–water interface. *Food Hydrocolloids* **2008**,
18 *22*, 387–402.
- 19 (45) Nelson, A.; Wang, D.; Koynov, K.; Isa, L. A multiscale approach to the adsorption of
20 core–shell nanoparticles at fluid interfaces. *Soft matter* **2015**, *11*, 118–129.
- 21 (46) Gyulai, G.; Kiss, É. Interaction of poly (lactic-co-glycolic acid) nanoparticles at fluid
22 interfaces. *Journal of Colloid and Interface Science* **2017**, *500*, 9–19.



- 1 (47) Ferdous, S.; Ioannidis, M. A.; Henneke, D. Adsorption kinetics of alkanethiol-capped
2 gold nanoparticles at the hexane–water interface. *Journal of Nanoparticle Research*
3 **2011**, *13*, 6579–6589.
- 4 (48) Graham, D.; Phillips, M. Proteins at liquid interfaces: I. Kinetics of adsorption and
5 surface denaturation. *Journal of colloid and interface science* **1979**, *70*, 403–414.
- 6 (49) Muntz, I.; Waggett, F.; Hunter, M.; Schofield, A. B.; Bartlett, P.; Marenduzzo, D.; Thi-
7 jssen, J. H. Interaction between nearly hard colloidal spheres at an oil-water interface.
8 *Physical Review Research* **2020**, *2*, 023388.



Data Availability Statement

View Article Online
DOI: 10.1039/D4NA00280F

This manuscript presents both the raw data and the analysis derived from processing the data. The raw data can be found in the Figure 1 of main manuscript. Figures 2-4 present the derived analysis from the raw data. Details on the processing steps used to generate this analysis are provided in the supplementary information.

